Journal of Alloys and Compounds 883 (2021) 160753

Contents lists available at ScienceDirect

Journal of Alloys and Compounds

journal homepage: www.elsevier.com/locate/jalcom

Insight to agglomeration and chemical reactions of $CoAl_2O_4$ inoculants in IN718 processed by selective laser melting

I-Ting Ho[a,*], Kai-Chun Chang[b], Dhruv Tiparti[a], An-Chou Yeh[b], Sammy Tin[a,*]

[a] Department of Mechanical, Materials and Aerospace Engineering, Illinois Institute of Technology, Chicago, IL, USA
[b] Department of Materials Science and Engineering, National Tsing Hua University, Hsinchu, Taiwan, R.O.C.

ARTICLE INFO

Article history:
Received 8 April 2021
Received in revised form 3 June 2021
Accepted 5 June 2021
Available online 8 June 2021

Keywords:
Selective laser melting
Inconel 718
Inoculant
Agglomeration
Microstructure

ABSTRACT

The investigation aims to clarify the influence of scan parameters on the morphology and phase constitution of $CoAl_2O_4$ inoculants in Inconel 718 (IN718) superalloy processed by selective laser melting (SLM). Gas atomized IN718 powder feedstock was uniformly blended with 0.2 wt% of $CoAl_2O_4$ flakes and processed with a range of laser scan parameters to understand the effect of the inoculant additions on microstructure. Similar to the reactions observed in investment cast Ni-superalloys, the $CoAl_2O_4$ particles were found to chemically react with elemental Al, Cr, and Ti present in the melt pool of IN718 and become reduced into Al_2O_3, Cr_2O_3, and TiO_2 oxides after the SLM process. Analyses of single melt pool beads revealed the existence of Co-rich metallic particles distributed along the surface of the oxides. However, since SLM processing involves remelting of the previously deposited layers to minimize the occurrence of porosity, this results in the dissolution of the Co-rich metallic particles that form when the $CoAl_2O_4$ particles are reduced in the melt pool. As such, the ability of the metallic Co particles to contribute to grain refinement becomes limited during SLM processing. Furthermore, the inoculant particles were found to agglomerate along the scan direction. The underlying mechanisms can be attributed to the Marangoni convection following the moving center of laser beam. It was found that decreasing energy density and increasing scan speed can effectively reduce the size and number density of the agglomerated oxide particles. Faster laser scan velocities lead to reduced convective flow within the melt pool and reduce the tendency for agglomeration. However, the reduced magnitude of energy input limited the time over which the $CoAl_2O_4$ particles could react with the melt pool. This led to the formation of lack of fusion defects and incomplete chemical reaction between $CoAl_2O_4$ and IN718 after the SLM process. The effectiveness of $CoAl_2O_4$ inoculant particles on grain refinement in as-built SLM IN718 microstructures is strongly dependent on the melt pool physics and laser scan conditions.

1. Introduction

The advent of fusion based additive manufacturing (AM) has resulted in transformational improvements on manufacturing and enabled ultimate design freedom as it possesses the flexibility to fabricate intricate components that are difficult to be produced by conventional methods such as casting, forging, and traditional machining [1]. Among the fusion based AM process, selective laser melting (SLM) is one of the popular techniques to process the pre-alloyed powder layer-by-layer through scanning a laser beam in a path that defines the geometry desired. SLM processed Ni-base superalloy components for gas turbine engines have received considerable attention in recent years as significant economic and design related benefits can be attained. It should be noted that, however, the characteristically high thermal gradient and rapid cooling rate incurred during SLM processing is often associated with the formation of a fine, columnar-grained microstructure with strong anisotropy along the [001] or [101] direction. Since the crystallographic anisotropy may persist even following heat-treatment of the as-built material and affect mechanical properties such as tensile strength, fatigue threshold, and creep rupture life [2–9], the applicability of AM parts may be limited.

For conventional castings, numerous studies have been conducted to minimize the extent of microstructural anisotropy during solidification by facilitating a columnar-to-equiaxed transition through the use of inoculants [10–13]. According to the correlation proposed by Hunt et al. [14] and Gaumman et al. [15], the thermal

* Corresponding authors.
E-mail addresses: iho@hawk.iit.edu (I.-T. Ho), tin@iit.edu (S. Tin).

https://doi.org/10.1016/j.jallcom.2021.160753
0925-8388/

gradient exhibits a correlation as a function of nuclei density and solid-liquid interface velocity which is shown in the follows:

$$G = \frac{1}{n+1}\sqrt[3]{\frac{-4\pi N_0}{3ln[1-\phi]}}\cdot(a\cdot V)^{1/n} \quad (1)$$

where G is the thermal gradient, N_0 is the nuclei density, ϕ is the equiaxed grain fraction, V is the solid-liquid interface velocity, and a and n are material constants. Eq. (1) indicates that for a given G and V, increasing nuclei density enhances the fraction of equiaxed grains. The Interdependence model [16–19] further elucidated the contributions of inoculants on the formation of microstructure during solidification. Assuming the thermal gradient is aligned with the direction of grain growth, the distance separating each nucleation event (d_{gs}) can be divided into three distinct length scales: (1) x_{cs}, the required length for grain growth before sufficient constitutional supercooling (ΔT_{cs}) is generated that activate nearby nucleation sites; (2) x_{dl}, the length of solute diffusion field from the solidification interface to where ΔT_{cs} is equal to the nucleant potency, ΔT_n; (3) x_{sd}, the distance between possible nucleation sites within the melt pool. Namely, the d_{gs} can be derived as

$$d_{gs} = x_{cs} + x_{dl} + x_{sd} = \frac{Dz\Delta T_n}{VQ} + \frac{4.6D}{V}*\left(\frac{C_i^* - C_o}{C_l^*(1-k)}\right) + x_{sd} \quad (2)$$

Here, D stands for the solute diffusion coefficient, z is a term proportional to the thermal gradient G, Q stands for the solute growth restriction factor, V stands for the solid-liquid interface velocity, C_o is the alloy composition, C_l^* is the liquid composition at the interface, and k is the partition coefficient.

The nucleant potency (ΔT_N), i.e. the undercooling required for nucleation on inoculants or solute clusters, is defined as [20]:

$$\Delta T_N = 4\gamma/(\Delta S_v d) \quad (3)$$

where ΔS_v is the entropy of fusion, γ is the interfacial energy, and d is the particle size. It could be seen that a proper selection of inoculants with crystallographic planes that are coherent to the matrix can effectively reduce ΔT_n as lower interfacial energy could be obtained; a reduced magnitude of d_{gs} hence accounts for more pronounced heterogeneous nucleation resulting in an equiaxed-grained structure. Effective inoculant particles include a wide variety of precipitates including oxides, borides, and carbides that possess high melting points. The particular use of inoculants has been reported to facilitate the formation of equiaxed grains in AM processed aluminum alloys [17,21–24], ferrous alloys [25–30], titanium alloys [31], and nickel alloys [32–35].

$CoAl_2O_4$ was commonly used to promote an equiaxed-grained structure in investment cast Ni-superalloys [36–44]. The interior surfaces of investment molds are often coated with a mixture of $CoAl_2O_4$ and zirconia. As the investment mold is filled with molten metal, various reactions may occur between $CoAl_2O_4$ and the elemental Al, Ti, Cr in the superalloy melt. These reactions reduce the $CoAl_2O_4$ and lead to the formation of solid elemental Co on the surface of shell mold. Since the Co particles possess a higher melting temperature than Ni-superalloys and have a crystallographic structure that is nearly identical to that of the Ni-superalloy, the solid Co particles that form contribute to heterogeneous grain nucleation during solidification. Our previous study has confirmed the ability of $CoAl_2O_4$ to facilitate grain refinement and enhance tensile properties and creep resistance for SLM processed IN718 [45]. $CoAl_2O_4$ inoculant particles were pre-mixed with IN718 powder and processed via SLM. The sequence of reactions and mechanisms responsible for inoculant induced grain refinement in conventional castings appears to be drastically different when compared to SLM processing. The high energy laser, rapid solidification, multiple remelting of the deposited materials, and flow and convection of the melt pool can all affect the effectiveness of inoculants and the resulting microstructural evolution during SLM processing. Moreover, the convective flow of the melt pool during SLM may contribute to agglomeration of inoculants or reacted particles that can ultimately impact the resulting mechanical properties of the material. Previous studies have shown the agglomeration of reinforcing particles that exhibited a strong dependence on processing parameters in several ODS alloys or metal matrix composites (MMC) [46–48], but the behavior of $CoAl_2O_4$ particles that chemically react and become reduced is still not well understood. For these reasons, this investigation aims to elucidate the influence of scan parameters on the microstructural evolution of SLM processed IN718 mixed with micro-sized $CoAl_2O_4$ in terms of agglomeration and phase constitution.

Table 1
Nominal composition of IN718 powder used for SLM in wt% and at%.

	Ni	Co	Cr	Fe	Al	Cu	Ti	Si	Mn	Mo	Nb	C
wt%	Bal.	0.5	19	17.75	0.6	0.2	0.9	0.18	0.18	3.05	5.1	0.04
at%	Bal.	0.5	21.3	18.5	1.3	0.2	1.1	0.4	0.2	1.1	3.2	0.2

2. Experimental procedures

2.1. Materials

Gas atomized IN718 powder was supplied by Chia Yi Steel Inc., Taiwan, with D_{10} = 15 µm, D_{50} = 30 µm, and D_{90} = 52 µm. The composition characterized by ICP atomic emission spectroscopy was provided by the supplier and is shown in Table 1. As shown in Fig. 1(a), the particles were mostly spherical, although some irregularly shaped particles were also observed. The $CoAl_2O_4$ particles were supplied by Alfa Aesar Inc. with D_{10} = 0.3 µm, D_{50} = 2.6 µm, and D_{90} = 6.1 µm. For this investigation, 0.2 wt% of $CoAl_2O_4$ flakes was blended with IN718 powder using a roller mill; the blending procedure was carried out with a speed of 130 rpm for 1 h. The secondary electron (SE) images shown in Fig. 1(c) revealed a random distribution of $CoAl_2O_4$ particles that adhered to the surface of IN718 powder after blending.

2.2. SLM process and post-processing

An in-house SLM machine at the National Tsing Hua University equipped with a YLR-AC-500 W Ytterbium fiber laser with a beam size of 58 µm was used for this study. Selective laser melting was carried out under an Ar atmosphere with oxygen levels below 2000 ppm. A 50 µm thick layer of pre-mixed IN718 powder with $CoAl_2O_4$ particles was spread onto a pure Ni baseplate. Samples were produced from a range of laser powers and scan speeds listed in Table 2 and were marked as C1, C2, C3, C4, and C5, respectively. The hatch distance was fixed at 100 µm and a zig-zag scan pattern with no rotation was used to process the successive layers. The volumetric energy density for each parameter was also included in Table 2 which is defined as follows:

$$\text{Volumetric energy density } (J/mm^3) = \frac{Laser\ power\ (W)}{Scan\ speed\ (mm/s)\times Hatch\ \ distance\ (\mu m)\times Layer\ thickness\ (\mu m)}\times 10^6 \quad (4)$$

Several cubes with the dimension of 1 cm^3 as well as single pass beads were produced using the assigned parameters. Afterwards, the cube samples were detached from the base-plate for characterization while the single bead samples were characterized by sectioning the baseplate into 5 mm thickness using electrical discharge machining. Samples were subjected to solution heat-treatment (SHT) for better phase characterization of inoculants. SHT was conducted

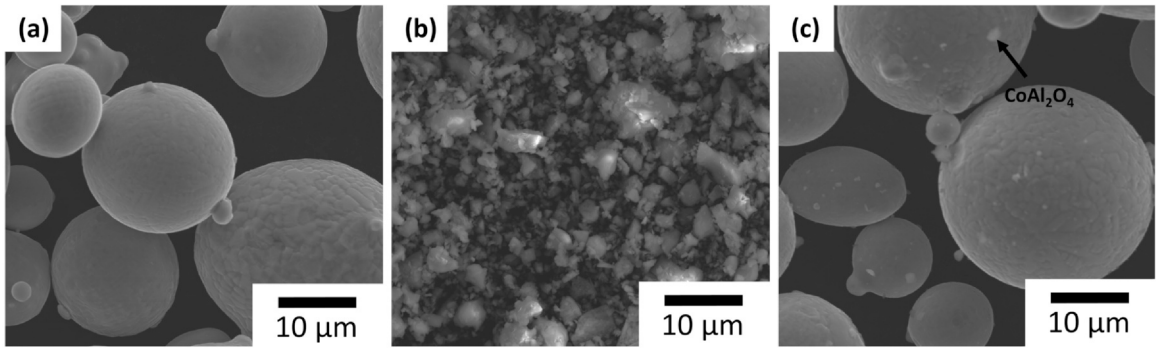

Fig. 1. SEM images showing the powders of (a) IN718 and (b) $CoAl_2O_4$ used for the SLM process. The morphology of IN718 powder blended with 0.2 wt% of $CoAl_2O_4$ flakes are shown in (c).

Table 2
Scan parameters used for the SLM process. The layer thickness and hatch distance were fixed at 50 µm and 100 µm, respectively. The volumetric energy density for each condition was also included.

	C1	C2	C3	C4	C5
Laser power (W)	220	220	220	220	260
Scan speed (mm/s)	800	1000	1200	1400	945
Energy density (J/mm^3)	55	44	36.7	31.4	55

at 1100 °C, which is above the solvus temperature of δ phase, for 2 h, followed by air-cooling to ambient temperature [49].

2.3. Sample preparation and characterization

Specimens for microstructural characterization were prepared using standard metallographic procedures with a final polishing step with 0.05 µm alumina suspension and were electrolytically etched using a 15% phosphoric acid solution. Microstructures were observed under a field emission scanning electron microscope (FESEM, JEOL JSM-6701F), equipped with a Bruker energy dispersive X-ray spectroscopy (EDS) detector. Both secondary electron (SE) and backscattered electron (BSE) micrographs were taken under 15 kV to reveal the morphology and elemental distribution within the inoculants, respectively; the middle of the cube samples (5 mm away from the base plate) was observed for comparison. Discrete nano-sized oxides within the matrix were observed and the area fraction was estimated using ImageJ software. The cellular spacing as well as particle size of inoculants were measured using Nanomeasure software.

The grain structure of the sample was characterized using a JEOL JSM 5900-LV scanning electron microscope (SEM) equipped with an Oxford Instruments Nordlys Nano electron backscatter diffraction (EBSD) detector. Specimens were mounted in resin and prepared using standard metallographic polishing techniques with a final polishing step with 0.06 µm colloidal silica. An area of 1 mm^2 was collected to do the EBSD analysis using an accelerating voltage of 20 kV and a 2 µm step size. The collected data was analyzed using Channel 5-HKL software.

Since only a small mass fraction of $CoAl_2O_4$ was blended with the powder feedstock, quantitative analysis of the oxide particles present in the microstructure was performed by phase extraction and electrolytic dissolution of the IN718 matrix material. Individual samples along with a Pt anode were immersed into a solution consisting of 30 ml of HCl, 325 ml of methanol, and 7 g of tartaric acid; voltage was adjusted to maintain a constant current at 0.12 A at ambient temperature. The extraction procedure was conducted for 2 days until sufficient particles were collected for phase characterization. The collected powder was analyzed using a Bruker D2 X-ray diffractometer, with CuKα radiation and power settings of 30 kV and 10 mA. Each scan was carried out across the angular range (2θ) from 20° to 100° with a step size of 0.01° and a dwell time of 4 s

3. Results

3.1. Observations of single pass beads

Fig. 2 depicts the optical micrographs showing the top view of single pass beads. By taking the average along a distance of 5 mm, the melt pool width was measured to be 108 ± 3 µm, 94 ± 6 µm, 86 ± 16 µm, 75 ± 15 µm, 105 ± 8 µm for C1 to C5, respectively. It could be seen that the average width of melt pool gradually decreased as the energy density decreased from 55 J/mm^3 to 31.4 J/mm^3. Simultaneously, the deviation of melt pool width was measured to be 10 µm, 17 µm, 22 µm, 16 µm, and 17 µm for C1 to C5, respectively, showing a more heterogeneous feature of melt pool when processed using higher scan speeds. The large deviation in melt pool processed by high scan speeds corresponds to the formation of defects characteristic of humping and discontinuous advance of the melt pool as shown in Fig. 2.

The corresponding SE images showing the cross-sections of single pass beads are displayed in Fig. 3. Similar to the observations in Fig. 2, the height of the melt pool appeared to respond to the applied scan parameters and decrease with decreasing energy density. Interestingly, agglomerations of the inoculants were observed to take place largely on the surface of solidified single pass deposits. Fig. 4(a) and (b) shows the general features of agglomerated oxides on the surface of single pass beads; the corresponding compositions were analyzed by EDS and were presented in Table 3. The morphologies of inoculant particles located on the surfaces of the melt pools appeared to be irregular and were distinctly different from the shape of $CoAl_2O_4$ powder after blending with the IN718 powder feedstock. Additionally, it should be noted that the size of oxide particles observed on the surface of the melt pools was found to be larger than the d_{90} of initial $CoAl_2O_4$ powder, suggesting that agglomeration might have occurred during the first scan. Fig. 4(b) reveals that the agglomerated oxide particle comprised a mixture of oxides that consist of $CoAl_2O_4$ and other oxides as a result of chemical reaction. EDS chemical analysis showed that the reacted portion was enriched with Al, Ti, and Cr and deficient in Co, while the unreacted portion exhibited a stoichiometric composition consistent with $CoAl_2O_4$. This would appear to indicate that the $CoAl_2O_4$ inoculant additions were only partially reduced by the reactive elements in the melt pool. It should be noted that the standard deviation for each component did not largely change the phase constitution, indicating that the reactions taking place between the inoculants and IN718 matrix were independent of the scan parameters.

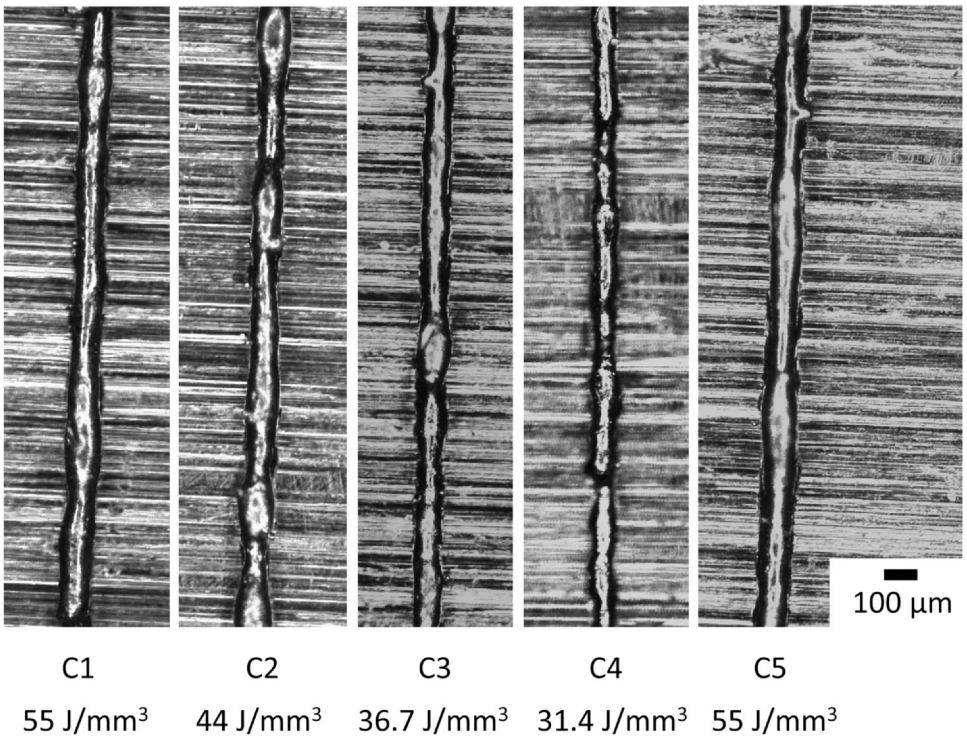

Fig. 2. Optical micrographs showing the top view of single pass beads for IN718 with $CoAl_2O_4$ processed by various conditions. The corresponding condition and energy density applied were provided below each figure.

In addition to the oxides, some metallic particles with average sizes smaller than 1 µm were found to be randomly dispersed on the surface of agglomerated oxide, as indicated in Fig. 4(b); the EDS analysis confirmed that these particles are enriched in Co and other compositions from IN718 matrix including Ni, Fe, and Cr. Fig. 4(c) and (d) show the cellular dendritic microstructure within the single pass beads. Although the majority of non-metallic oxide particles were found on the surface of melt pool, nano-scale oxides (~100 nm) were still observed to be mostly distributed along the cellular dendritic boundaries. The distribution and morphology of these oxides are consistent with those reported in other studies [45,50].

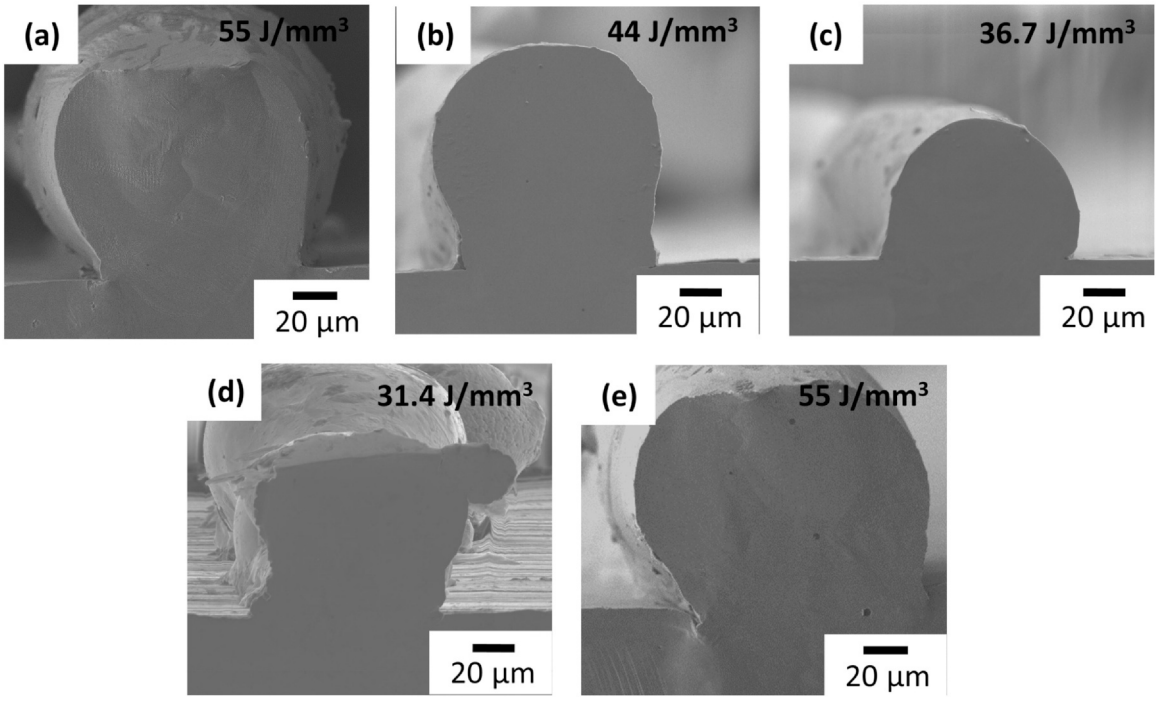

Fig. 3. SE images showing the morphologies of cross-section for single pass beads of IN718 with $CoAl_2O_4$ processed by (a) C1, (b) C2, (c) C3, (d) C4, and (e) C5, respectively. The corresponding energy density was indicated at the right top of each figure.

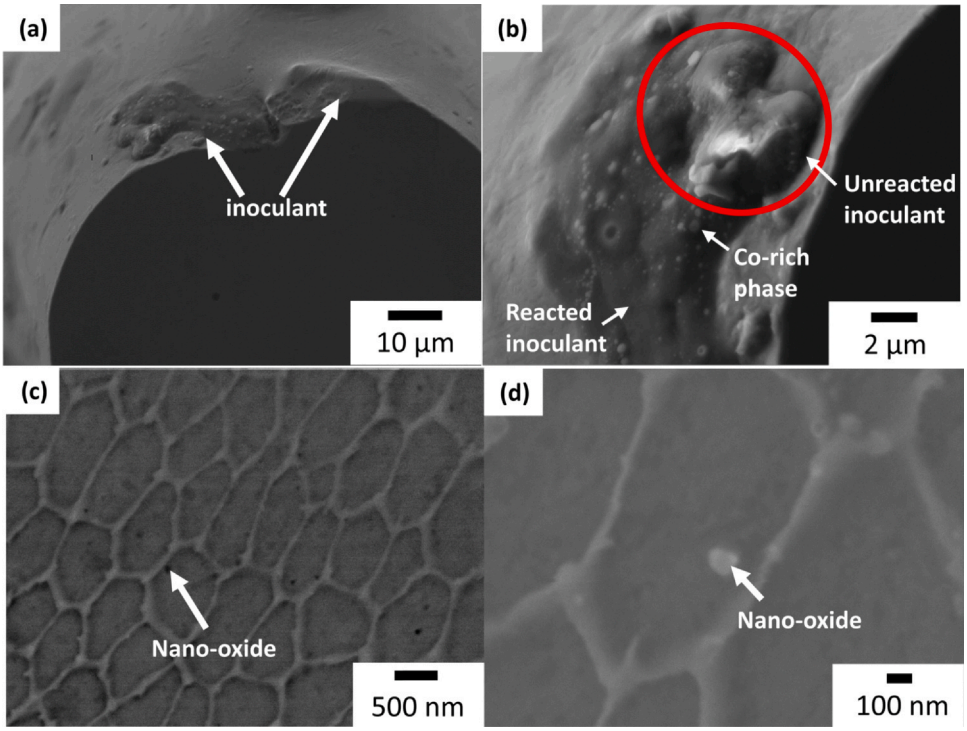

Fig. 4. SEM micrographs showing the miscellaneous features of inoculant particles for the single pass beads of IN718 with $CoAl_2O_4$: (a) SE image showing the distribution of inoculant particles; (b) SE image showing morphology of inoculant particles; (c) BSE image showing nano-oxides and cellular dendritic structure present within the single pass beads; (d) SE image showing morphology of nano-scale oxides.

Table 3
EDS results for particular features present in Fig. 4(b). The average and standard deviation were taken from the same features in samples processed by C1 to C5.

at%	Ni	Fe	Cr	Co	Al	Ti	Mo	Nb	O
IN718 matrix	54.1 ± 3.5	17 ± 0.1	17.3 ± 0.3	0.9 ± 0.1	2.2 ± 1	1.5 ± 0.3	1.7 ± 0.1	2.6 ± 0.2	2.9 ± 1.6
Reacted inoculant	3.7 ± 1.8	1.1 ± 0.7	3 ± 0.5	0.4 ± 0.1	22.6 ± 2.7	4.8 ± 1.5	0.1 ± 0	0.4 ± 0.2	63.7 ± 2.4
Unreacted inoculant	4.2 ± 3	1.2 ± 1	3 ± 2.5	14.6 ± 3	26.3 ± 2.8	1.3 ± 0.8	0.2 ± 0.1	0.4 ± 0.3	48.8 ± 8.6

3.2. Microstructure characterization for cube samples

Fig. 5(a-c) show the microstructures of as-built sample processed by C1 with respect to transverse direction (TD), build direction (BD), and scan direction (SD). Since no rotation of scan pattern was applied in present study, distinct microstructures would be expected between the vertical sections along the TD (xz plane) and SD (yz plane). In particular, the inoculants were found to be randomly distributed within the matrix and possess an average size of 15 µm when the section along BD and TD (xz plane) was observed (see Fig. 5(a)). This observation supports that the $CoAl_2O_4$ particles were uniformly distributed throughout the IN718 powder before processing as the inoculants did not segregate to certain layers or scan tracks. The microstructure taken along BD and SD (yz plane), on the other hand, exhibited large numbers of agglomerates that had become elongated along the SD; some of the elongated particles were observed to possess lengths that exceeded 100 µm, which is significantly larger than the d_{90} of initial $CoAl_2O_4$ powder (see Fig. 5(b)). A similar elongated morphology was observed along the TD and SD (xy plane), Fig. 5(c). It could be seen that the agglomeration mainly occurred along the SD. The elongated morphology associated with the agglomerated oxide particles seemed to be a function of the scan track direction.

Varying the laser scan parameters appeared to directly affect the agglomeration of the oxides and strongly influenced their morphologies. Fig. 6(a-d) show the microstructures of as-built samples processed by C2, C3, C4, and C5 with respect to BD and SD (yz plane), respectively. Since the same mixture of powders was utilized for all processing parameters, it could be expected that the uniform distribution of inoculants would be observed along BD and TD (xz plane). However, the morphologies of agglomerated oxides observed along BD and SD seemed to possess a strong dependence on processing parameters. Table 4 contains a statistical assessment of the number of agglomerated oxides larger than d_{90} of initial $CoAl_2O_4$ powder as well as the largest length of agglomerated oxides for Fig. 5(b) and Fig. 6(a-d). Over an area of 1.4 mm × 1 mm, the largest length of the inoculant particle was found to decrease from 164 µm to 80 µm and coincided with a slight increase in the overall number of particles from 18 to 24 when the energy density decreased from 55 J/mm^3 (C1) to 44 J/mm^3 (C2). As the energy density further decreased to 36.7 J/mm^3 (C3), the number of agglomerated oxide particles decreased significantly to 6, and the largest length of the inoculant particles decreased to 37 µm. Similar to the C3 sample, the C4 samples showed the same number of agglomerated oxide particles, but the length was notably smaller at 14 µm and approached the d_{90} values measured from the initial $CoAl_2O_4$ powder. The reduction in the size of the non-metallic particles as a function of energy density was also associated with lack of fusion defects and the presence of large pores with the sizes >100 µm, as shown in Fig. 6(b) and (c).

Surprisingly, the comparison between the C1 sample and the C5 sample revealed that there was a large decrease in the size of agglomerated oxides from 164 µm to 68 µm as scan speeds increased from 800 mm/s to 945 mm/s, despite having the same energy density. A similar trend was observed when sectioned with respect to TD and SD (xy plane), Fig. 7. The largest size of oxide particles was

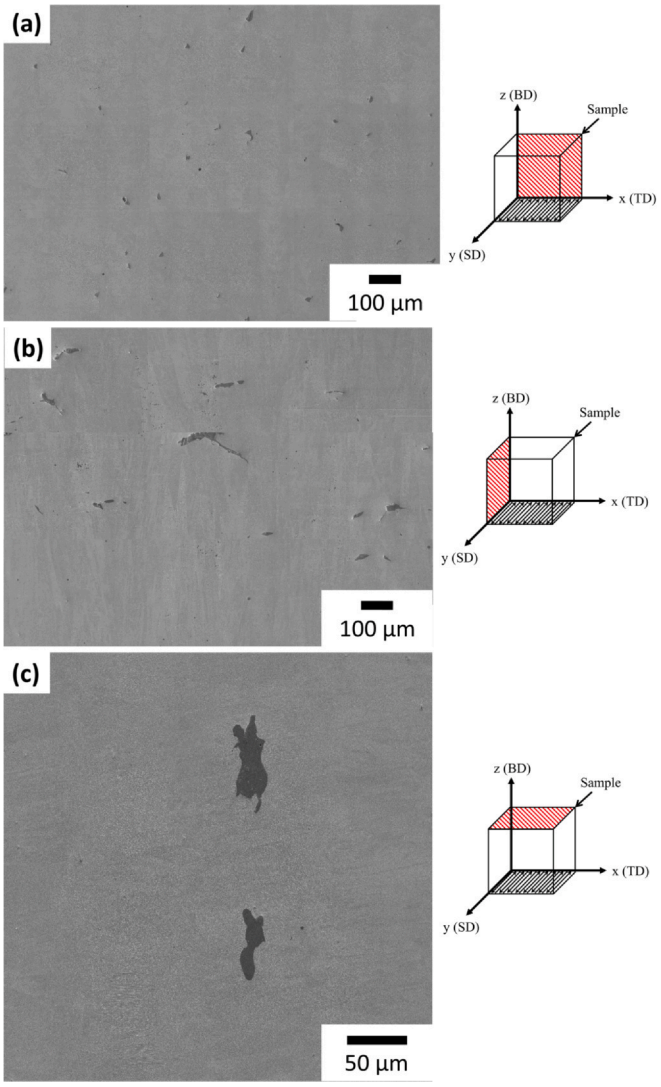

Fig. 5. Microstructures of as-built IN718 with $CoAl_2O_4$ processed by C1 along the (a) transverse direction (TD) and build direction (BD), (b) scan direction (SD) and build direction (BD), and (c) transverse direction (TD) and scan direction (SD), respectively. The black particles were identified as inoculants. Note that the black arrows present in the basal plane of the coordinates represent the zig-zag scan pattern used for the SLM process.

measured to be 90 µm, 37 µm, 17 µm, 9 µm, and 57 µm in samples processed by C1 to C5, respectively. It could be seen that the degree of the oxide agglomeration exhibited the same trend as that in the yz plane. The size of agglomerated oxides was significantly reduced in C2, C3, and C5 samples and finally approached the d_{90} of the initial $CoAl_2O_4$ powder in the C4 sample. These findings confirm that both energy density and scan speed may strongly impact the resulting particle morphologies.

To effectively capture the effects of the non-uniform spatial distribution of agglomerated particles on the resulting grain structure, EBSD IPF Z maps for C1 sample and C2 sample were characterized with respect to BD and SD and are displayed in Fig. 8. For comparison, the regions where inoculants were heavily agglomerated in samples C1 and C2 were also included. In the C1 sample, the average grain aspect ratio associated with regions without (Fig. 8(a)) and with (Fig. 8(b)) heavily agglomerated oxide particles was measured to be 2.72 and 2.86, respectively, and did not vary significantly. In sample C2, there was a more significant variation in the grain aspect ratio and the values varied from 2.57 to 1.78 for Fig. 8(c) and (d), respectively. Equiaxed grains appeared to obfuscate the initial columnar grained features and significantly reduced the grain aspect ratio in C2 sample when the area fraction of agglomerated oxides increased. The findings clearly suggest that the non-uniform distribution of agglomerated oxides might have contributed to the formation of an inhomogeneous grain structure that became more pronounced when scan parameters were modified to reduce the energy density.

The change in the inoculant morphology induced by the scan parameters was reflected on not only the morphology but also the resulting phase constitution. Fig. 9 shows the microstructures of the inoculant particles in C1, C3, and C5 samples, respectively; the average composition for each feature was summarized in Table 5. Similar to the observations in single pass beads, both agglomerated particles and un-agglomerated particles were composed of a mixture of non-metallic oxides enriched with Al, Cr, and Ti and metallic particles enriched with Co and Ni. Unlike the inoculants on the surface in the single pass beads specimens, no metallic particles were observed to reside along the interface between the oxide particles and the IN718 matrix.

In the C1 sample, the $CoAl_2O_4$ inoculant was completely reduced and fully reacted to form non-Co containing oxides when successive layers of powder were melted along with the underlying substrate to form a melt pool. As the laser scan parameters were modified to reduce the magnitude of the energy density (e.g. C3), the constitution of the agglomerated oxides changed to consist of a mixture of unreacted $CoAl_2O_4$ particles along with Al, Ti, and Cr-rich oxides. The EDS results shown in Table 5 confirmed that the composition of unreacted particles is consistent with those present in the single pass bead specimens. Interestingly, the C5 sample also revealed the presence of partially reacted inoculant particles. These partially reacted inoculant particles were largely composed of Ti-rich oxides and unreacted $CoAl_2O_4$. To better understand the impact of processing parameters on the resulting microstructure, the cellular dendritic microstructure of the as-built samples was observed under higher magnification for each condition, and the results are shown in Fig. 10. The average cellular spacing was measured to be 1020 nm, 990 nm, 760 nm, 700 nm, and 960 nm for samples processed using the C1 to C5 conditions, respectively. The variations in the measured spacings show a strong dependence on both the energy densities and scan speeds. Discrete nano-scale oxides were also observed to be randomly distributed within the dendritic microstructure. These nano-scale oxide particles possessed the same morphology as those found in the single bead experiments.

Results from the XRD phase characterization of the oxides that had been chemically extracted from the as-built samples are displayed in Fig. 11 (a). Chemical phase extraction and the corresponding XRD diffraction pattern for the C1 sample containing no $CoAl_2O_4$ inoculant have also been included to benchmark the phases present. For this sample, the diffraction pattern consists largely of peaks corresponding to Laves phase and (Nb, Ti)C carbides. The presence of these phases is also in agreement with observations for both conventional cast and wrought and additively manufactured IN718 in previous studies [51–54]. In addition to Laves precipitates and carbides, the diffraction pattern corresponding to the extractions from C1 sample containing $CoAl_2O_4$ inoculant exhibits peaks that correspond to Al_2O_3. The absence of $CoAl_2O_4$ is consistent with the observations in Fig. 9(a) and (d). The diffraction peaks corresponding to the oxide particles became more apparent after removing the contributions from Laves phase. Phase extractions were also performed on the samples subjected to the SHT which fully solutioned all of the Laves phase precipitates. The corresponding diffraction patterns, Fig. 11 (b), clearly reveal the presence of Al_2O_3, (Nb, Ti)C, Cr_2O_3, and TiO_2. The higher relative intensity associated with the peaks corresponding to Al_2O_3 suggests that the largest fraction of oxides are likely Al_2O_3. Similar to the C1 sample, the C4 sample containing $CoAl_2O_4$ also exhibits a mixture of oxides Al_2O_3,

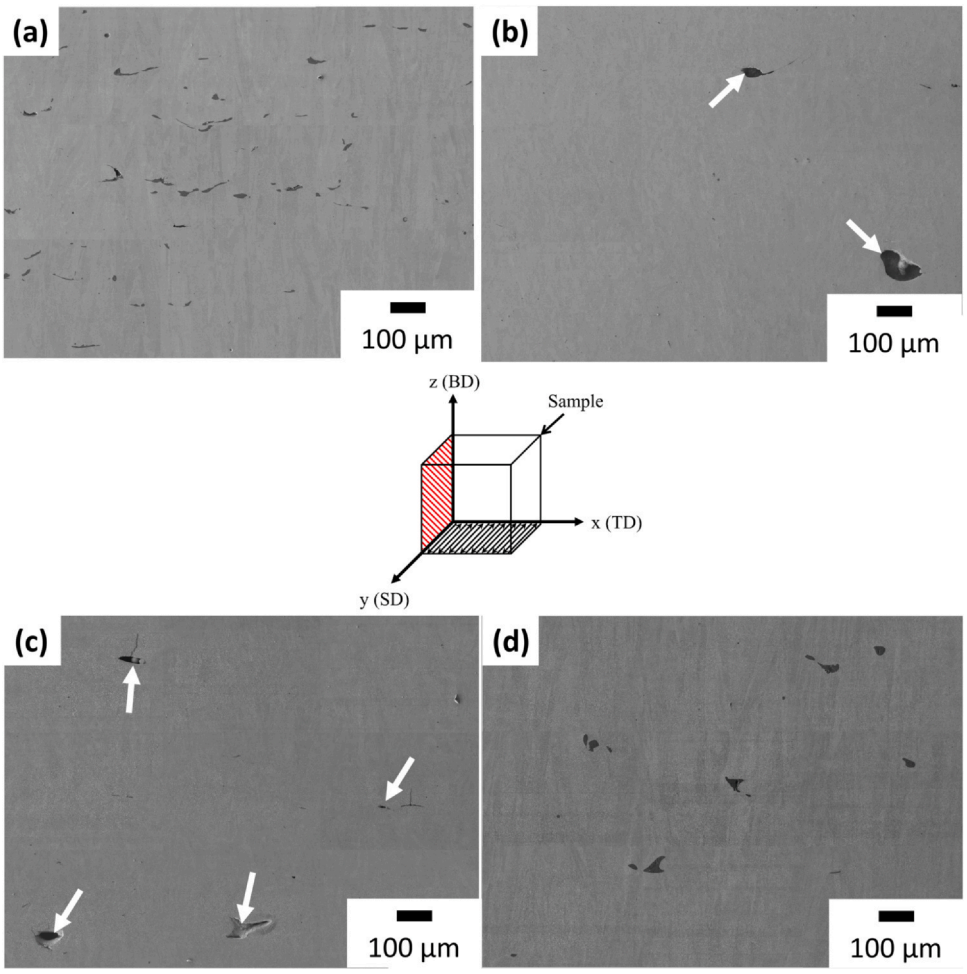

Fig. 6. Microstructures of as-built IN718 with $CoAl_2O_4$ processed by (a) C2, (b) C3, (c) C4, and (d) C5 along the BD and SD, respectively. Note that the area captured for (a-d) is the same as Fig. 5(b). The porosities are indicated by white arrows particularly.

Cr_2O_3, and TiO_2. The same peaks attained from both conditions clearly suggest that the same level of reactions may have taken place within the inoculants during the SLM process. The absence of unreacted $CoAl_2O_4$ that was observed in Fig. 9(b) and (e) in the C4 sample might be attributed to its comparatively low volume fraction among the reacted oxides and carbides.

Fig. 12 shows the microstructures of extracted particles obtained from the C1 samples processed with $CoAl_2O_4$. In particular, Fig. 12 (a-c) display the microstructure of extracted particles under the as-built state while Fig. 12 (d-e) display the microstructure of extracted particles after the SHT. In the as-built state, both needle-shaped Laves accompanied with carbides as well as reacted oxides were revealed by different contrast under the BSE mode. After the SHT, the morphologies of carbides and reacted oxides became more obvious (see Fig. 12 (d) and (e)); the nano-scale oxides were also found under higher magnification which possessed a spherical morphology, as shown in Fig. 12 (f). The EDS analysis confirmed that the composition of reacted oxides is the same as the average composition shown in Table 5.

Table 4
Summary of number of agglomerated oxides larger than d_{90} of $CoAl_2O_4$ as well as the largest length of agglomerated oxide characterized in Fig. 5(b) and Fig. 6(a-d).

	C1	C2	C3	C4	C5
Numbers of particles larger than d_{90} of $CoAl_2O_4$	18	24	6	6	14
Largest length of agglomerated particle (µm)	164	80	37	14	68

4. Discussion

4.1. Agglomeration of $CoAl_2O_4$ inoculant particles

As aforementioned in Fig. 4(a), the agglomeration of inoculant particles to form large non-metallic particles was observed to occur on the surface of single pass melt beads. The agglomeration of inoculants appeared to align along the scan direction leading to a non-uniform distribution of agglomerated oxides whose maximum size was approximately 27 times larger than the initial d_{90} of the $CoAl_2O_4$ powder that was blended with the powder feedstock in the C1 sample (see Fig. 5(b) and Fig. 5(c)). The underlying mechanism of agglomeration can likely be attributed to the Marangoni convection induced by the non-uniform temperature distribution of temperature [55,56]. The convection driven by the thermocapillary force can be defined by a non-dimensional Marangoni number (Ma) that follows:

$$\mathrm{Ma} = \frac{d\gamma}{dT}\frac{dT}{dx}\frac{L^2}{\eta a} \tag{5}$$

where γ is the surface tension, $(\frac{d\gamma}{dT})$ is the surface tension coefficient, $(\frac{dT}{dx})$ is the temperature gradient from the center of melt pool, η is the viscosity, a is the thermal diffusivity, and L is the characteristic length. Numerical studies predicting the melt pool dynamic have demonstrated that the temperature and surface tension coefficient as a function of distance to the moving center of laser beam enhance

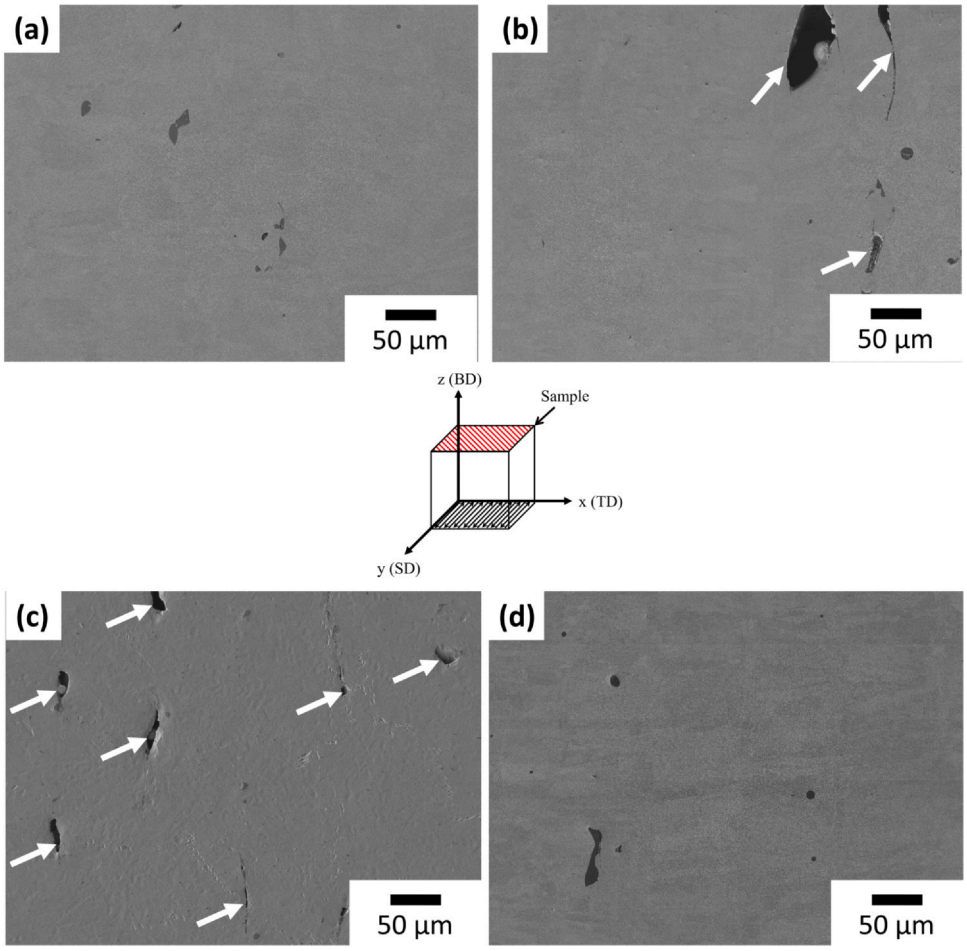

Fig. 7. Microstructures of as-built IN718 with $CoAl_2O_4$ processed by (a) C2, (b) C3, (c) C4, and (d) C5, respectively, along the TD and SD. The porosities are indicated by white arrows particularly.

the Marangoni number and lead to an either radially outward or radially inward surface flow, depending on the level of impurities such as oxygen or sulfur [32,57–59]. The convection thus carries the hot metal as well as inoculants towards the certain directions, and the center of convection follows the moving center of the laser.

Computational modeling studies have shown that the temperature of a laser induced melt pool during the AM process can exceed 2000°C, which surpasses the melting temperature of $CoAl_2O_4$ (1955 °C) [1,11,59]. The inoculant particles that are being transported by the Marangoni convection may partially melt and agglomerate with other inoculant particles along the SD. Additionally, since the density of $CoAl_2O_4$ is approximately half of that of IN718, the resulting buoyant force also drives the oxide particles towards the surface of the melt pool. This additional driving force likely explains the preferential presence of agglomerated oxides on the surface of the single pass beads, as shown in Fig. 4(a). As successive layers or beads are deposited, the laser with high energy densities may exacerbate this phenomenon by forming a melt pool that extends well into the previously deposited material and pulls the already agglomerated oxides to the surface of the new melt pool. This process may occur multiple times and gradually build up the size of the agglomerated oxides until they become sufficiently large where their movements ultimately become restricted and they can no longer be pulled up to the surface of the melt pool. This would be consistent with the observations of a non-uniform distribution of agglomerated particles shown in Fig. 5(b) and Fig. 5(c).

The observations in Fig. 6 and Fig. 7 clearly demonstrated that both the size and number of agglomerated oxides were largely decreased when scan parameters were modified to reduce the energy density and increase the laser scan speed, as seen in samples C3 and C4. The variation in the morphologies of the single pass beads that were deposited, Fig. 2, indicate that the energy density of applied scan parameters exerts a positive correlation to the size of melt pool. The higher energy densities also impact the temperature of melt pool. Thermal modeling has demonstrated that the overall temperature of melt pool increases with increasing energy density due to a higher proportion of energy directed into the powder bed [59–61]. Since it has been reported that the viscosity of molten metals is inversely proportional to the root of temperature [62], larger Marangoni numbers corresponding to increased convective flow are also expected when parameters are adjusted to increase the energy density. With a physically larger melt pool, a correspondingly higher density of oxides is likely to be entrained within the melt pool and leads to an increased probability of agglomeration. This is consistent with the observations from this investigation as the higher energy density laser scan parameters also resulted in an increase of the size and number of agglomerated oxides from sample C4 to C1.

The reduced size and number of agglomerated oxides in C5 sample can be attributed to the increased laser scan speed and correspondingly smaller melt pool. For Ni-superalloys, the cellular/dendrite arm spacing (λ_1) decreases with increasing cooling rate ($\dot{T}$), and the relationship between λ_1 and $\dot{T}$ can be derived as follows [63]:

$$log\lambda_1 = -0.26\log(\dot{T}) + \log 134.43 \quad (6)$$

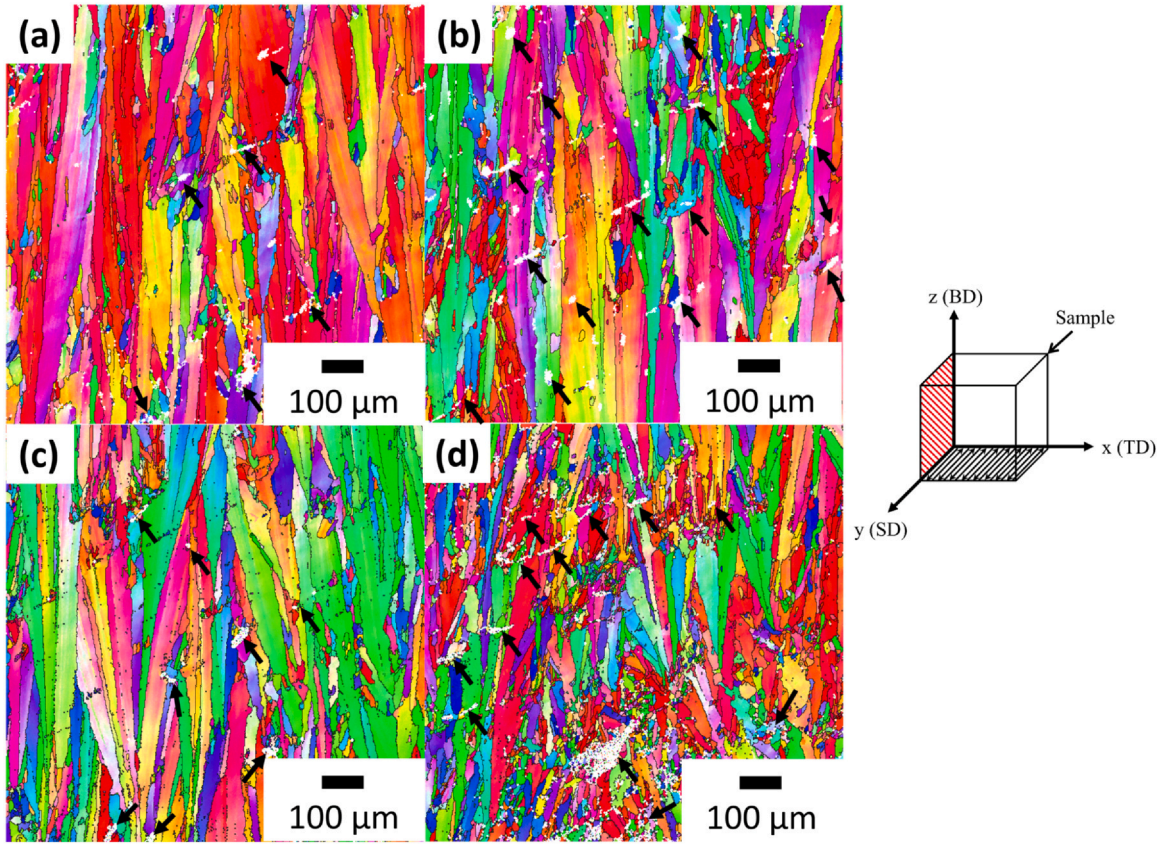

Fig. 8. EBSD IPF Z maps for the as-built samples processed by (a-b) C1 and (c-d) C2, respectively, with respect to the BD and SD. Note that the IPF Z maps for regions where heavily agglomerated oxide particles were identified for C1 sample and C2 sample are shown in (b) and (d), respectively. The agglomerated inoculants are indicated by the black arrows.

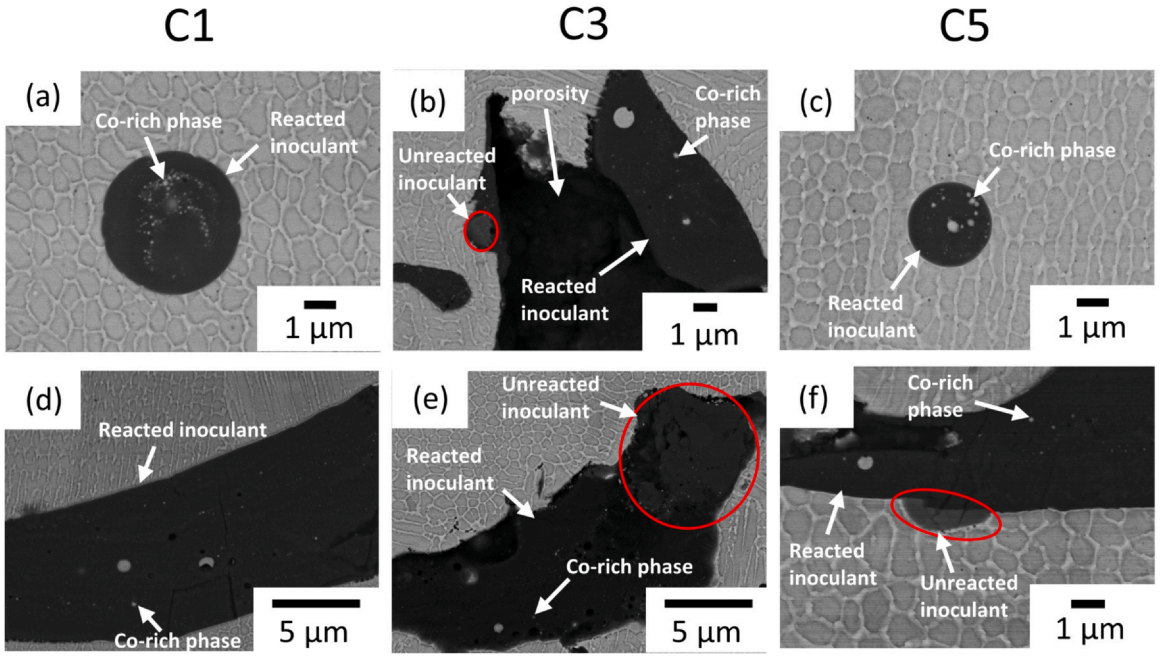

Fig. 9. BSE images showing the general features of (a-c) un-agglomerated inoculant particles and (d-f) heavily agglomerated inoculant particles in as-built IN718. Note that (a) and (d) represent the inoculants in sample processed by C1; (b) and (e) represent the inoculants in sample processed by C3; (c) and (f) represent the inoculants in sample processed by C5.

Using the cellular spacing measured from Fig. 10, the cooling rate in C1 sample is estimated to be 1.3 times slower than that in C5 sample while 4.4 times slower than that in C4 sample. The increased laser scan speeds result in an increased cooling rate during solidification of the melt pool which is consistent with results from finite element modeling studies [60,64]. Since the higher cooling rates reduce the time interval over which the liquid melt pool is able to exist, the oxide particle movements are limited and the

Table 5
EDS results for particular features present in Fig. 9. The average and standard deviation were taken from the same features in samples processed by C1 to C5. Note that the composition for unreacted inoculants in C5 sample is separated from others as different composition was detected. 5 data points were included to estimate the average and standard deviation for the unreacted inoculants in C5 sample.

at%	Ni	Fe	Cr	Co	Al	Ti	Mo	Nb	O
IN718 matrix	52.4 ± 0.7	18.2 ± 0.2	18.3 ± 0.6	1 ± 0.1	1.3 ± 0.3	1.4 ± 0.1	2 ± 0.1	3.1 ± 0.4	2.2 ± 0.3
Reacted inoculant	0.6 ± 0.2	0.2 ± 0.1	2.1 ± 0.3	0.2 ± 0	26.5 ± 0.8	6.9 ± 0.4	0.1 ± 0	0.1 ± 0.1	61.6 ± 3.4
Unreacted inoculant	3.8 ± 2.1	1.6 ± 0.9	2.1 ± 0.9	15.2 ± 0.9	27.9 ± 0.5	0.6 ± 0.3	0.3 ± 0.1	0.3 ± 0.1	48.2 ± 4
Unreacted inoculant (in C5)	1.3 ± 0.2	0.7 ± 0.1	1.5 ± 0.3	17.2 ± 1.3	29.9 ± 3.3	2.7 ± 0.6	0.2 ± 0.1	0.2 ± 0.1	46.5 ± 2.8

probability of agglomeration can be reduced as evidenced in the C5 sample. The findings are also consistent with the microstructure of the C4 samples where agglomeration was nearly eliminated by reducing the energy density and utilizing a high scan speed.

4.2. Microstructure evolution of $CoAl_2O_4$ inoculant particles

In the present study, the microstructural observations from the single bead deposits (Fig. 4) and cube samples (Fig. 9 and Fig. 10) combined with XRD of the extracted particles have confirmed that the $CoAl_2O_4$ inoculant particles that were initially blended with the IN718 powder feedstock were reduced within the melt pool to form various oxides rich in Al, Ti, and Cr along with Co-rich metallic particles. Once formed, the compositions of reduced oxide particles were found to be unchanged when successive layers were processed. Previous studies have shown that $CoAl_2O_4$ undergoes a similar reduction process in Ni-superalloys during the investment casting [37,38]. In IN718, $CoAl_2O_4$ particles may follow the chemical reactions with Al, Cr, and Ti in the molten alloy that are described as follows [37]:

$$CoO{\cdot}Al_2O_3 + 2/3Al = 4/3Al_2O_3 + Co \quad (7)$$

$$3(CoO{\cdot}Al_2O_3) + 2Cr = 3Co + Cr_2O_3 + 3(Al_2O_3) \quad (8)$$

$$CoO{\cdot}Al_2O_3 + 1/2Ti = Al_2O_3 + Co + 1/2TiO_2 \quad (9)$$

The chemical potential for (7), (8), (9) was estimated to be − 250 kJ, − 100 kJ, and − 180 kJ at 1300 °C, respectively, and does not vary significantly with the change in temperature [37]. The chemical reactions strongly suggested that the $CoAl_2O_4$ inoculants were reduced into Al_2O_3, Cr_2O_3, and TiO_2 following the same reactions as those observed in investment cast Ni-superalloys during the SLM process. The higher atomic fraction of Al and Ti in reacted oxides compared to that of Cr also corresponds to the high magnitude of the chemical potential for the formation of Al_2O_3 and TiO_2. The same reactions are also responsible for the presence of solid Co-rich particles as a by-product of these reactions.

Interestingly, the Co-rich phase characterized on the surface of inoculants shown in Fig. 4(b) was found to dissolve and become incorporated in the IN718 samples when additional layers of material are deposited using a melt pool that extends beyond the depth of the deposited layer, Fig. 9. For investment cast Ni-superalloys, the pouring temperature of the melt generally does not exceed the melting temperature of Co (1490 °C) and hence the solid Co particles that form on the surface of shell mold can survive and promote heterogeneous grain nucleation during solidification. During the SLM process, however, the characteristically high melt pool temperature as well as Marangoni convection may melt the reacted metallic Co particles. As a result, the effects of $CoAl_2O_4$ inoculants on SLM processed samples would be expected to be different from that of conventionally casting samples as grain nucleation on solid Co particles is no longer likely to occur.

The unreacted $CoAl_2O_4$ inoculants present in single bead deposits can be attributed to the intrinsically fast cooling rate during the SLM process. It is estimated that the cooling rate of melt pool could approach 10^5-10^8 K/s during the SLM process [65–68]. Additionally, the thermal conductivity of $CoAl_2O_4$ is generally below 10 $Wm^{-1}K^{-1}$, which is approximately 2.5 times smaller than that of IN718, at 1500 K [69,70]. The reduced rate of heat transfer as well as limited time interval for diffusion of Al, Ti, and Cr in the melt pool may inhibit the chemical reactions between $CoAl_2O_4$ and IN718 leading to a small fraction of unreacted particles after the first scan. On the other

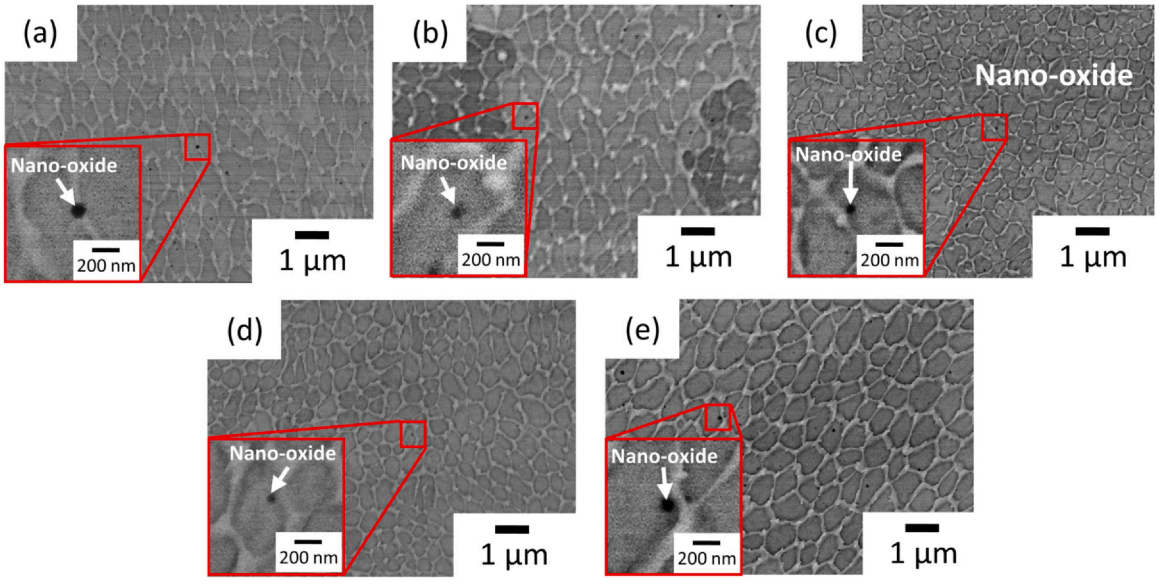

Fig. 10. BSE images showing the cellular structure in samples processed by (a) C1, (b) C2, (c) C3, (d) C4, and (e) C5, respectively. Note that the black particles within cellular dendrites were identified as nano-scale oxides.

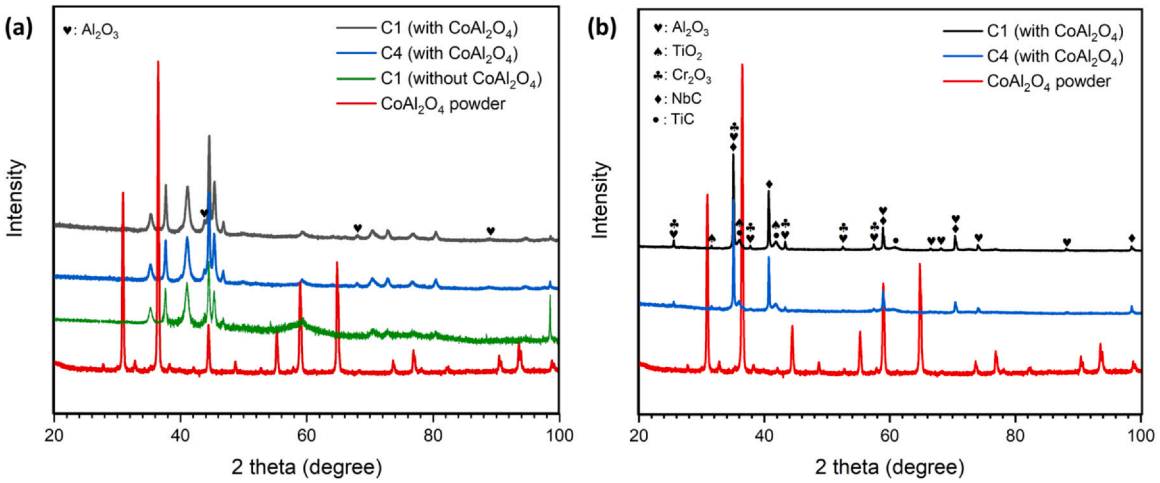

Fig. 11. XRD spectra for (a) as-built and (b) solution heat-treated IN718 with $CoAl_2O_4$, respectively. Both chemically extracted C1 sample and C4 sample were analyzed. The spectra for $CoAl_2O_4$ powder and as-built IN718 without $CoAl_2O_4$ were also included for comparison.

hand, when successive layers were processed, all of the particles were observed to become fully reduced in the C1 sample while some unreacted or partially reacted $CoAl_2O_4$ was still identified in samples processed by C2-C5. Similar to the underlying mechanisms that facilitate agglomeration, a high energy density ensures remelting of the previously deposited material as the melt pool extends through the deposited layer. When a penetrating melt pool is combined with a relatively low laser scan speed, the probability that $CoAl_2O_4$ particles can be fully reduced is high as the time interval over which the reaction can occur is largely dependent on the scan speed. This is consistent with the presence of partially reacted $CoAl_2O_4$ particles observed in the microstructures of sample C3 and C5, Fig. 9.

Results from the present study clearly demonstrate a range of microstructures can form during SLM processing of IN718 containing $CoAl_2O_4$ inoculant particles. The microstructures are sensitive to the range of processing parameters as the Marangoni convection within the melt pool can result in agglomeration of fine oxides and form large non-metallic particles. With decreasing energy density and increasing scan speed, both the size and number of agglomerated oxide particles can be effectively minimized owing to the reduced recirculation times. As a trade-off, porosity and lack-of-fusion defects may occur within the microstructure as the energy input and melt pool penetration depth are reduced. The chemical reactions that result in decomposition of $CoAl_2O_4$ into Al_2O_3, Cr_2O_3, TiO_2, and Co-rich particles during the SLM process were found to be consistent with those in investment cast Ni-superalloys. Due to the melt pool penetration and remelting of the previously deposited layers, the solid Co-rich particles that formed during the reduction of $CoAl_2O_4$ are reincorporated back into the melt pool and are unable to serve as heterogeneous grain nucleation sites during solidification. The present study illustrates a clear need to better understand the underlying mechanisms associated with the formation of microstructure during SLM processing of IN718 with $CoAl_2O_4$ inoculant particles and the importance of the laser scan parameters. In order to minimize agglomeration of oxides and enable the Co-rich particles to heterogeneously nucleate grains during solidification, laser scan parameters must be optimized to minimize the melt pool penetration depth and the extent of convective flow.

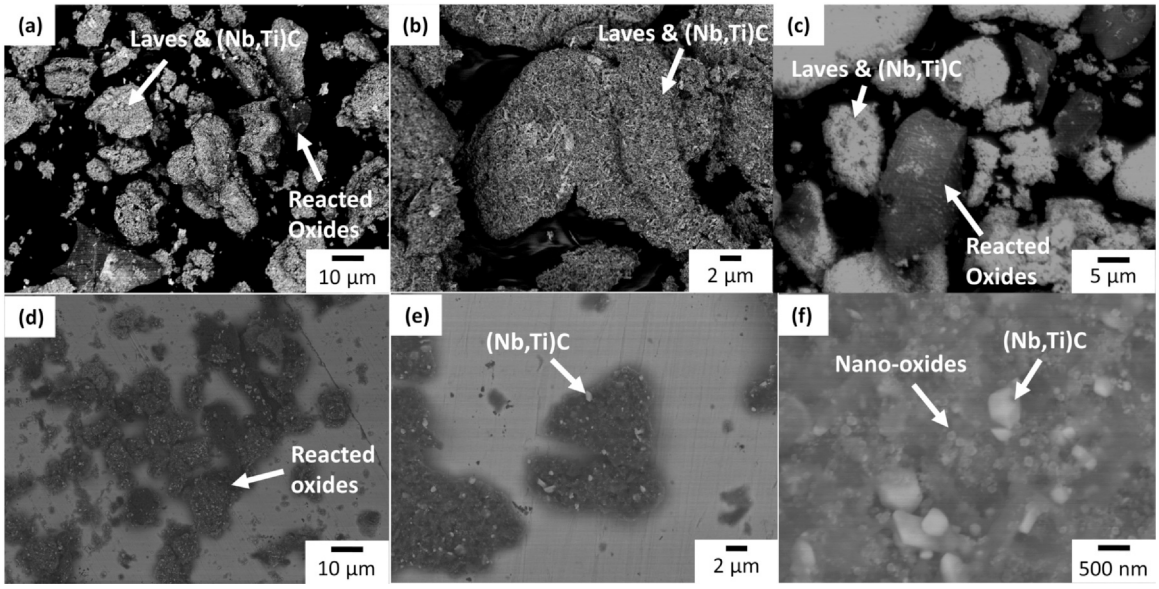

Fig. 12. The BSE micrographs showing the distinct features of chemically extracted C1 sample containing $CoAl_2O_4$ inoculant. Note that (a)-(c) show the extracted powder from the as-built samples while (d)-(f) show the powder from the samples after SHT.

5. Conclusion

During the first scan associated with melting of the powder feedstock, chemical reactions occurred between $CoAl_2O_4$ particles and IN718 powder leading to the reduction of $CoAl_2O_4$ to form Co-rich metallic particles along with various oxides including Al_2O_3, Cr_2O_3, and TiO_2. Since the melt pool associated with successive layers extends beyond the deposited layer of new powder and re-melts the underlying beads that have been previously deposited onto the build, the Co-rich metallic particles that form due to the chemical reduction of $CoAl_2O_4$ melt and are incorporated back into the melt pool. Without the presence of solid, metallic Co-rich particles, the ability of the $CoAl_2O_4$ inoculants to facilitate heterogeneous nucleation during SLM processing of IN718 might be limited. Furthermore, it was found that the phase compositions and particle morphology of the non-metallic oxides that form as a result of the $CoAl_2O_4$ additions exhibit a strong dependence on the SLM scan parameters. The following conclusions can be drawn based on the observations on samples produced by different scan parameters.

1. Increasing energy density increases the recirculation times of melt pool due to the higher melt pool temperature and lower viscosity. The more intense convection facilitates more oxide particles with low densities to agglomerate onto the surface of melt pool. The larger size of the melt pool induced by higher energy density also contributes to increasing the extent of agglomeration as more non-metallic particles are able to interact during each scan.
2. Despite using the same energy density, higher scan speeds contribute to an increase in cooling rate and reduce the overall solidification times of the deposited material. Shorter solidification time thereby leads to a reduced flow within the melt pool and mitigates the degree of agglomeration.
3. The high cooling rates and short solidification time associated with the high laser scan speeds can also result in an incomplete chemical reaction between the $CoAl_2O_4$ and the IN718 melt pool following a single pass. This leads to the formation of a microstructure that contains a mixture of unreacted $CoAl_2O_4$ alongside the reduced Al_2O_3, Cr_2O_3, and TiO_2 oxides. The extent of melt pools that leads to significant remelting of previously deposited layers enables eventual reduction of the unreacted $CoAl_2O_4$. For the scan parameters associated with lower energy densities and higher cooling rates, limited remelting of the previously deposited layers combined with insufficient time interval over which the reaction can occur accounts for the presence of unreacted $CoAl_2O_4$ within the as-built microstructure.

CRediT authorship contribution statement

I-Ting Ho: Conceptualization, Methodology, Investigation, Validation, Data curation, Visualization, Writing - original draft**. Kai-Chun Chang:** Investigation, Validation. **Dhruv Tiparti**: Methodology. **An-Chou Yeh:** Writing - review & editing, Resources. **Sammy Tin:** Writing - review & editing, Supervision.

Declaration of Competing Interest

The authors declare that they have no known competing financial interests or personal relationships that could have appeared to influence the work reported in this paper.

Acknowledgments

This work was supported by the National Science Foundation (NSF), USA CMMI # 1663068 and the Ministry of Science and Technology (MOST), Taiwan MOST108-2218-E007-009.

References

[1] T. DebRoy, H.L. Wei, J.S. Zuback, T. Mukherjee, J.W. Elmer, J.O. Milewski, A.M. Beese, A. Wilson-Heid, A. De, W. Zhang, Additive manufacturing of metallic components – process, structure and properties, Prog. Mater. Sci. 92 (2018) 112–224, https://doi.org/10.1016/j.pmatsci.2017.10.001
[2] J. Strößner, M. Terock, U. Glatzel, Mechanical and microstructural investigation of nickel-based superalloy IN718 manufactured by selective laser melting (SLM), Adv. Eng. Mater. 17 (2015) 1099–1105, https://doi.org/10.1002/adem.201500158
[3] K.N. Amato, S.M. Gaytan, L.E. Murr, E. Martinez, P.W. Shindo, J. Hernandez, S. Collins, F. Medina, Microstructures and mechanical behavior of Inconel 718 fabricated by selective laser melting, Acta Mater. 60 (2012) 2229–2239, https://doi.org/10.1016/j.actamat.2011.12.032
[4] D. Deng, R.L. Peng, H. Brodin, J. Moverare, Microstructure and mechanical properties of Inconel 718 produced by selective laser melting: sample orientation dependence and effects of post heat treatments, Mater. Sci. Eng. A 713 (2018) 294–306, https://doi.org/10.1016/j.msea.2017.12.043
[5] T. Trosch, J. Strößner, R. Völkl, U. Glatzel, Microstructure and mechanical properties of selective laser melted Inconel 718 compared to forging and casting, Mater. Lett. 164 (2016) 428–431, https://doi.org/10.1016/j.matlet.2015.10.136
[6] D. Deng, J. Moverare, R.L. Peng, H. Söderberg, Microstructure and anisotropic mechanical properties of EBM manufactured Inconel 718 and effects of post heat treatments, Mater. Sci. Eng. A 693 (2017) 151–163, https://doi.org/10.1016/j.msea.2017.03.085
[7] M.D. Sangid, T.A. Book, D. Naragani, J. Rotella, P. Ravi, A. Finch, P. Kenesei, J.S. Park, H. Sharma, J. Almer, X. Xiao, Role of heat treatment and build orientation in the microstructure sensitive deformation characteristics of IN718 produced via SLM additive manufacturing, Addit. Manuf. 22 (2018) 479–496, https://doi.org/10.1016/j.addma.2018.04.032
[8] M.M. Kirka, P. Fernandez-Zelaia, Y. Lee, P. Nandwana, S. Yoder, O. Acevedo, D. Ryan, Mechanical performance of a Non-weldable Ni-base superalloy: inconel 738 fabricated by electron beam melting, Miner. Met. Mater. Ser. (2020) 1075–1084, https://doi.org/10.1007/978-3-030-51834-9_105
[9] M. Seifi, A.A. Salem, D.P. Satko, R. Grylls, J.J. Lewandowski, Effects of post-processing on microstructure and mechanical properties of SLM-processed IN-718, Miner. Met. Mater. Ser. (2018) 515–526, https://doi.org/10.1007/978-3-319-89480-5_33
[10] G.L. deFaria, A.S. Leite, The effect of casting speed and the fraction of Al5%Ti1%B inoculant on the microstructure and mechanical properties of the AA5052 aluminum alloy produced by the direct chill process, Mater. Res. 21 (2018), https://doi.org/10.1590/1980-5373-mr-2017-0997
[11] A.L. Greer, A.M. Bunn, A. Tronche, P.V. Evans, D.J. Bristow, Modelling of inoculation of metallic melts: application to grain refinement of aluminium by Al-Ti-B, Acta Mater. 48 (2000) 2823–2835, https://doi.org/10.1016/S1359-6454(00)00094-X
[12] R. Vaz Penna, L.N. Bartlett, R. O'Malley, Influence of TiN additions on the microstructure of a lightweight Fe–Mn–Al steel, Int. J. Met. 14 (2020) 342–355, https://doi.org/10.1007/s40962-019-00373-6
[13] M. Bedel, K.O. Tveito, M. Založnik, H. Combeau, M.M. 'Hamdi, A model study of the impact of the transport of inoculant particles on microstructure formation during solidification, Comput. Mater. Sci. 102 (2015) 95–109, https://doi.org/10.1016/j.commatsci.2015.01.028
[14] J.D. Hunt, Steady state columnar and equiaxed growth of dendrites and eutectic, Mater. Sci. Eng. 65 (1984) 75–83, https://doi.org/10.1016/0025-5416(84)90201-5
[15] M. Gäumann, C. Bezençon, P. Canalis, W. Kurz, Single-crystal laser deposition of superalloys: processing-microstructure maps, Acta Mater. 49 (2001) 1051–1062, https://doi.org/10.1016/S1359-6454(00)00367-0
[16] D.H. Stjohn, M. Qian, M.A. Easton, P. Cao, The interdependence theory: the relationship between grain formation and nucleant selection, Acta Mater. 59 (2011) 4907–4921, https://doi.org/10.1016/j.actamat.2011.04.035
[17] M.H. Ghoncheh, M. Sanjari, A.S. Zoeram, E. Cyr, B.S. Amirkhiz, A. Lloyd, M. Haghshenas, M. Mohammadi, On the microstructure and solidification behavior of new generation additively manufactured Al-Cu-Mg-Ag-Ti-B alloys, Addit. Manuf. 37 (2021) 101724, https://doi.org/10.1016/j.addma.2020.101724
[18] A. Prasad, L. Yuan, P.D. Lee, D.H. StJohn, The interdependence model of grain nucleation: a numerical analysis of the nucleation-free zone, Acta Mater. 61 (2013) 5914–5927, https://doi.org/10.1016/j.actamat.2013.06.015
[19] A. Prasad, L. Yuan, P. Lee, M. Patel, D. Qiu, M. Easton, D. StJohn, Towards understanding grain nucleation under additive manufacturing solidification conditions, Acta Mater. 195 (2020) 392–403, https://doi.org/10.1016/j.actamat.2020.05.012
[20] A.L. Greer, J.H. Perepezko, F. Franks, B. Cantor, R.W. Cahn, Grain refinement of alloys by inoculation of melts, Philosophical Transactions of the Royal Society A: Mathematical, Physical and Engineering Sciences, 2003, https://doi.org/10.1098/rsta.2002.1147
[21] J.H. Martin, B.D. Yahata, J.M. Hundley, J.A. Mayer, T.A. Schaedler, T.M. Pollock, 3D printing of high-strength aluminium alloys, Nature 549 (2017) 365–369, https://doi.org/10.1038/nature23894
[22] L. Xi, P. Wang, K.G. Prashanth, H. Li, H.V. Prykhodko, S. Scudino, I. Kaban, Effect of TiB2 particles on microstructure and crystallographic texture of Al-12Si fabricated by selective laser melting, J. Alloy. Compd. 786 (2019) 551–556, https://doi.org/10.1016/j.jallcom.2019.01.327
[23] Y.K. Xiao, Z.Y. Bian, Y. Wu, G. Ji, Y.Q. Li, M.J. Li, Q. Lian, Z. Chen, A. Addad, H.W. Wang, Effect of nano-TiB2 particles on the anisotropy in an AlSi10Mg alloy processed by selective laser melting, J. Alloy. Compd. 798 (2019) 644–655, https://doi.org/10.1016/j.jallcom.2019.05.279

[24] J.H. Martin, B. Yahata, J. Mayer, R. Mone, E. Stonkevitch, J. Miller, M.R. O'Masta, T. Schaedler, J. Hundley, P. Callahan, T. Pollock, Grain refinement mechanisms in additively manufactured nano-functionalized aluminum, Acta Mater. 200 (2020) 1022–1037, https://doi.org/10.1016/j.actamat.2020.09.043
[25] V. Villaret, F. Deschaux-Beaume, C. Bordreuil, A solidification model for the columnar to equiaxed transition in welding of a Cr-Mo ferritic stainless steel with Ti as inoculant, J. Mater. Process. Technol. 233 (2016) 115–124, https://doi.org/10.1016/j.jmatprotec.2016.02.017
[26] B. AlMangour, D. Grzesiak, J.M. Yang, Scanning strategies for texture and anisotropy tailoring during selective laser melting of TiC/316L stainless steel nanocomposites, J. Alloy. Compd. 728 (2017) 424–435, https://doi.org/10.1016/j.jallcom.2017.08.022
[27] B. Li, B. Qian, Y. Xu, Z. Liu, J. Zhang, F. Xuan, Additive manufacturing of ultrafine-grained austenitic stainless steel matrix composite via vanadium carbide reinforcement addition and selective laser melting: formation mechanism and strengthening effect, Mater. Sci. Eng. A. 745 (2019) 495–508, https://doi.org/10.1016/j.msea.2019.01.008
[28] H. Ikehata, D. Mayweg, E. Jägle, Grain refinement of Fe Ti alloys fabricated by laser powder bed fusion, Mater. Des. 204 (2021) 109665, https://doi.org/10.1016/j.matdes.2021.109665
[29] A. Durga, N.H. Pettersson, S.B.A. Malladi, Z. Chen, S. Guo, L. Nyborg, G. Lindwall, Grain refinement in additively manufactured ferritic stainless steel by in situ inoculation using pre-alloyed powder, Scr. Mater. 194 (2021) 113690, https://doi.org/10.1016/j.scriptamat.2020.113690
[30] H. Ikehata, E. Jägle, Grain refinement of Fe-X alloys fabricated by laser powder bed fusion, Mater. Sci. Forum 1016 (2021) 580–586, https://doi.org/10.4028/www.scientific.net/MSF.1016.580
[31] M.J. Bermingham, D.H. StJohn, J. Krynen, S. Tedman-Jones, M.S. Dargusch, Promoting the columnar to equiaxed transition and grain refinement of titanium alloys during additive manufacturing, Acta Mater. 168 (2019) 261–274, https://doi.org/10.1016/j.actamat.2019.02.020
[32] A.T. Polonsky, N. Raghavan, M.P. Echlin, M.M. Kirka, R.R. Dehoff, T.M. Pollock, 3D Characterization of the Columnar-to-Equiaxed Transition in Additively Manufactured Inconel 718, in: 2020: pp. 990–1002. https://doi.org/10.1007/978-3-030-51834-9_97.
[33] T.-H. Hsu, K.-C. Chang, Y.-J. Chang, I.-T. Ho, S. Tin, C.-W. Li, K. Kakehi, C.-P. Chen, K.-K. Jen, H.-Y. Hsieh, A.-C. Yeh, Effect of Carbide Inoculants Additions in IN718 Fabricated by Selective Laser Melting Process, in: 2020: pp. 982–989. https://doi.org/10.1007/978-3-030–51834-9_96.
[34] Q. Han, Y. Gu, J. Huang, L. Wang, K.W.Q. Low, Q. Feng, Y. Yin, R. Setchi, Selective laser melting of Hastelloy X nanocomposite: effects of TiC reinforcement on crack elimination and strength improvement, Compos. Part B Eng. 202 (2020) 108442, https://doi.org/10.1016/j.compositesb.2020.108442
[35] Z. Zhang, Q. Han, S. Yang, Y. Yin, J. Gao, Laser powder bed fusion of advanced submicrometer TiB2 reinforced high-performance Ni-based composite, Mater. Sci. Eng. A 817 (2021) 141416, https://doi.org/10.1016/j.msea.2021.141416
[36] H. Matysiak, M. Zagorska, A. Balkowiec, B. Adamczyk-Cieslak, K. Dobkowski, M. Koralnik, R. Cygan, J. Nawrocki, J. Cwajna, K.J. Kurzydlowski, The influence of the melt-pouring temperature and inoculant content on the macro and microstructure of the IN713C Ni-based superalloy, Jom 68 (2016) 185–197, https://doi.org/10.1007/s11837-015-1672-5
[37] F. Binczyk, J. Śleziona, P. Gradoń, Modification of macrostructure of nickel superalloys with cobalt nanoparticles, Kompozyty 11 (2011) 49–54.
[38] Fang Jian, Yu Bin, Investigation of the surface grain refinement of superalloy castings, Jinshu Xuebao/Acta Metall. Sin. 18 (1982), https://doi.org/10.1007/978-94-009-7907-9_50
[39] F. Engineering, Criterion for selection the optimal physical and chemical properties of cobalt aluminate powder used in investment casting process, Arch. Foundry Eng. 9 (2009).
[40] N. Jacek, S. Dariusz, K. Krzysztof, M. Hubert, M. Maciej, Z. Waldemar, Influence of process parameters on cooling conditions in nickel base superalloy investment casting, Key Eng. Mater. (2015), https://doi.org/10.4028/www.scientific.net/KEM.641.124
[41] M. Zielińska, K. Kubiak, J. Sieniawski, Surface modification, microstructure and mechanical properties of investment cast superalloy, J. Achiev. Mater. Manuf. Eng. 35 (2009) 55–62.
[42] Ł. Rakoczy, M. Grudzień, R. Cygan, Influence of melt-pouring temperature and composition of primary coating of shell mold on tensile strength and creep resistance of Ni-based superalloy, J. Mater. Eng. Perform. 28 (2019) 3826–3834, https://doi.org/10.1007/s11665-018-3853-1
[43] A. Szczotok, J. Pietraszek, N. Radek, Metallographic study and repeatability analysis of γ' phase precipitates in cored, thin-walled castings made from IN713C superalloy!abstract, Arch. Metall. Mater. 62 (2017) 595–601, https://doi.org/10.1515/amm-2017-0088
[44] Rakoczy, M. Grudzień, R. Cygan, A. Zielińska-Lipiec, Effect of cobalt aluminate content and pouring temperature on macrostructure, tensile strength and creep rupture of inconel 713C castings, Arch. Metall. Mater. 63 (2018), https://doi.org/10.24425/123845
[45] I.-T. Ho, T.-H. Hsu, Y.-J. Chang, C.-W. Li, K.-C. Chang, S. Tin, K. Kakehi, A.-C. Yeh, Effects of CoAl2O4 inoculants on microstructure and mechanical properties of IN718 processed by selective laser melting, Addit. Manuf. 35 (2020) 101328, https://doi.org/10.1016/j.addma.2020.101328
[46] R.M. Hunt, K.J. Kramer, B. El-Dasher, Selective laser sintering of MA956 oxide dispersion strengthened steel, J. Nucl. Mater. 464 (2015) 80–85, https://doi.org/10.1016/j.jnucmat.2015.04.011
[47] B. AlMangour, M.S. Baek, D. Grzesiak, K.A. Lee, Strengthening of stainless steel by titanium carbide addition and grain refinement during selective laser melting, Mater. Sci. Eng. A 712 (2018) 812–818, https://doi.org/10.1016/j.msea.2017.11.126
[48] D. Dai, D. Gu, Influence of thermodynamics within molten pool on migration and distribution state of reinforcement during selective laser melting of AlN/AlSi10Mg composites, Int. J. Mach. Tools Manuf. 100 (2016) 14–24, https://doi.org/10.1016/j.ijmachtools.2015.10.004
[49] V. Beaubois, J. Huez, S. Coste, O. Brucelle, J. Lacaze, Short term precipitation kinetics of delta phase in strain free Inconel* 718 alloy, Mater. Sci. Technol. 20 (2004) 1019–1026, https://doi.org/10.1179/026708304225019830
[50] F. Yan, W. Xiong, E. Faierson, G.B. Olson, Characterization of nano-scale oxides in austenitic stainless steel processed by powder bed fusion, Scr. Mater. 155 (2018) 104–108, https://doi.org/10.1016/j.scriptamat.2018.06.011
[51] F. Brenne, A. Taube, M. Pröbstle, S. Neumeier, D. Schwarze, M. Schaper, T. Niendorf, Microstructural design of Ni-base alloys for high-temperature applications: impact of heat treatment on microstructure and mechanical properties after selective laser melting, Prog. Addit. Manuf. 1 (2016) 141–151, https://doi.org/10.1007/s40964-016-0013-8
[52] H. Qi, M. Azer, A. Ritter, Studies of standard heat treatment effects on microstructure and mechanical properties of laser net shape manufactured INCONEL 718, Metall. Mater. Trans. A 40 (2009) 2410–2422, https://doi.org/10.1007/s11661-009-9949-3
[53] L.L. Parimi, G. Ravi, D. Clark, M.M. Attallah, Microstructural and texture development in direct laser fabricated IN718, Mater. Charact. 89 (2014) 102–111, https://doi.org/10.1016/j.matchar.2013.12.012
[54] M.J. Donachie, Superalloys, second edition, A Technical Guide, America, 2002 https://doi.org/10.1361.
[55] C.R. Heiple, J.R. Rope, R.T. Stagner, R.J. Aden, Surface active element effects on the shape of gta, laser, and electron beam welds, Weld. J. 62 (1983).
[56] K.C. Mills, B.J. Keene, Factors affecting variable weld penetration, Int. Mater. Rev. 35 (1990) 185–216, https://doi.org/10.1179/095066090790323966
[57] M. Bayat, V.K. Nadimpalli, D.B. Pedersen, J.H. Hattel, A fundamental investigation of thermo-capillarity in laser powder bed fusion of metals and alloys, Int. J. Heat Mass Transf. 166 (2021) 120766, https://doi.org/10.1016/j.ijheatmasstransfer.2020.120766
[58] A. Queva, G. Guillemot, C. Moriconi, C. Metton, M. Bellet, Numerical study of the impact of vaporisation on melt pool dynamics in laser powder bed fusion - application to IN718 and Ti–6Al–4V, Addit. Manuf. 35 (2020) 101249, https://doi.org/10.1016/j.addma.2020.101249
[59] T.N. Le, Y.L. Lo, Z.H. Lin, Numerical simulation and experimental validation of melting and solidification process in selective laser melting of IN718 alloy, Addit. Manuf. 36 (2020) 101519, https://doi.org/10.1016/j.addma.2020.101519
[60] P. Yuan, D. Gu, D. Dai, Particulate migration behavior and its mechanism during selective laser melting of TiC reinforced Al matrix nanocomposites, Mater. Des. 82 (2015) 46–55, https://doi.org/10.1016/j.matdes.2015.05.041
[61] W. Yuan, H. Chen, T. Cheng, Q. Wei, Effects of laser scanning speeds on different states of the molten pool during selective laser melting: simulation and experiment, Mater. Des. 189 (2020) 108542, https://doi.org/10.1016/j.matdes.2020.108542
[62] R. Speiser, The physical properties of liquid metals, Mater. Sci. Eng. A 114 (1989), https://doi.org/10.1016/0921-5093(89)90864-2
[63] Y. Zhang, B. Huang, J. Li, Microstructural evolution with a wide range of solidification cooling rates in a Ni-based superalloy, Metall. Mater. Trans. A 44 (2013) 1641–1644, https://doi.org/10.1007/s11661-013-1645-7
[64] S. Liu, J. Zhu, H. Zhu, J. Yin, C. Chen, X. Zeng, Effect of the track length and track number on the evolution of the molten pool characteristics of SLMed Al alloy: numerical and experimental study, Opt. Laser Technol. 123 (2020) 105924, https://doi.org/10.1016/j.optlastec.2019.105924
[65] I.Gibson, D.Rosen, B.Stucker, Additive manufacturing technologies: 3D printing, rapid prototyping, and direct digital manufacturing, second edition, 2015. https://doi.org/10.1007/978-1-4939-2113-3.
[66] V. Popov, A. Katz-Demyanetz, M. Bamberger, Heat transfer and phase formation through EBM 3D-printing of Ti-6Al-4V cylindrical parts, Defect Diffus. Forum 383 (2018) 190–195, https://doi.org/10.4028/www.scientific.net/DDF.383.190
[67] N.E. Hodge, R.M. Ferencz, J.M. Solberg, Implementation of a thermomechanical model for the simulation of selective laser melting, Comput. Mech. 54 (2014) 33–51, https://doi.org/10.1007/s00466-014-1024-2
[68] D. Kong, C. Dong, X. Ni, L. Zhang, X. Li, Cellular size dependence on the strength of additively manufactured austenitic stainless steel, Mater. Lett. 279 (2020) 128524, https://doi.org/10.1016/j.matlet.2020.128524
[69] H. Hosaeus, A. Seifter, E. Kaschnitz, G. Pottlacher, Thermophysical properties of solid and liquid inconel 718 alloy, High Temp. High Press. 33 (2001) 405–410, https://doi.org/10.1068/htwu340
[70] Y. Ishitsuka, T. Ishikawa, R. Koborinai, T. Omura, T. Katsufuji, Comparative studies of the thermal conductivity of spinel oxides with orbital degrees of freedom, Phys. Rev. B 90 (2014) 224411, https://doi.org/10.1103/PhysRevB.90.224411